2015

A Study on the Effects of Using Redox Active Solvents on the Photophysical Properties of Hydride-Terminated Silicon Nanoparticles

Eunice Y. Lee
Portland State University

A Study on the Effects of Using Redox Active Solvents on the Photophysical Properties of Hydride-Terminated Silicon Nanoparticles

by

Eunice Y. Lee

An undergraduate honors thesis submitted in partial fulfillment of the

requirements for the degree of

Bachelor of Science

in

University Honors

and

Chemistry

Thesis Adviser

Dr. Andrea M. Goforth

Portland State University

2015

Table of Contents

Abstract

Silicon nanoparticles (Si NPs) have received much attention for their versatile applications in cell biology and medicine as *in vivo* molecular and cellular fluorescent markers. Recent studies have reported conversions of red-emitting silicon nanoparticles to blue-emitting particles. While blue emission is characteristic for 1-2 nm Si NPs, nanoparticles with larger radii that are closer to the Bohr exciton radius of bulk silicon (~ 4 nm) typically do not exhibit blue emission. Several studies have suggested that the oxidation of the surface of the silicon nanoparticles gives rise to the red-to-blue photoluminescence conversion. Herein, the oxidation and reduction potentials of 1-butanol, n-butylamine, and N,N-dimethylformamide (DMF) were measured and correlated to their ability to quench the photoluminescence of hydride-terminated Si NPs over time. The half-wave potentials of 1-butanol, n-butylamine, and DMF were measured to be 0.4416 V, 0.4979 V, and 0.7867 V. These half-wave potentials were studied on the basis that more electron-withdrawing solvents would result in a greater red-to-blue photoluminescence conversion and surface oxidation. Photoluminescence quenching studies showed that 1-butanol and DMF exhibited greater effects on the photophysical properties of the hydride-terminated Si NPs.

1. Introduction

1.1 Significance of Silicon Nanoparticles

1.1.1 Introduction to Nanoparticles

Nanoparticles are particles with characteristic compositions (inorganic and/or organic), functionalities, shapes, and sizes that range from 1 nm to 100 nm.[1] Different types of nanoparticles are engineered to exhibit specific optical, physical, and chemical properties such as chemical reactivity, electrical conductivity, and color.[2] The optical properties of nanoparticles have gained a significant amount of interest in both the art and science realms. The use of nanoparticles in art can be dated back to the 4th century a*nno domini*. The most famous example is the Lycurgus cup, a 4th century Roman glass cage cup fabricated with dichroic glass[a] (Figure 1). Another example of the use of nanoparticles in art is stained glass. The different pigments of the glass is controlled by the sizes and shapes of inorganic (metallic) nanoparticles such as gold and silver. These extraordinary optical properties of nanoparticles peaked the interests of researchers, and eventually led to the development of nanoparticles with specific applications in fields including energy production and medicine.[1–9]

Figure 1. The left image is of the Lycurgus cup when it is illuminated externally; the right image is of the cup when illuminated internally, normal to the surface of the cup (90°).[2] (Image provided by the British Museum,

[a] Glass that emits two different colors upon exposure to radiation such as light.

Nanoparticles with different metallic cores are being actively engineered to facilitate novel techniques in a wide range of applications including targeted drug delivery for cancer therapy, *in vivo* fluorescence imaging tools (cell labeling and biomolecule tracking)[10–12], and detection of chemical warfare agents.[1,4,5] Semiconductor nanoparticles, in particular, have gained much attention because of their distinctive photoconductive, electroluminescent, and size-dependent optical properties and versatile applicability as *in vivo* biomarkers.[b] However, semiconductor nanoparticles with indirect band gaps[c], such as silicon nanoparticles, have been proposed to be more efficient as biomarkers than those of heavy-metal based counterparts with direct band gaps such as cadmium (CdSe) and lead (PbS).

1.1.2 Silicon Nanoparticles: Properties and Applications

Silicon is naturally abundant, cost efficient, high in purity, and, as nanoparticles, lower in toxicity, exhibits broad absorption spectra, narrow emission bands, longer excited state lifetimes[d], and resistance to self-quenching[e] and photobleaching[f] over long periods of time.[1,13–15] These properties are expedient as fluorescence imaging tools for applications including cell labeling and biomolecule tracking. While semiconductor nanoparticles with direct band gaps, such as CdSe and PbS, have been useful as alternative fluorescent markers to organic dyes (*i.e.* rhodamine, fluorescein, phycoerythrin, *etc.*), recent studies have raised concerns about the toxicological issues[16] of using heavy-metal based quantum dots[g] in

[b] Measurable indicators of specific biological and pathogenic processes or responses to different health care interventions.[40]
[c] A band gap is classified as indirect when the bottom of the conduction band lies indirectly above the top of the valence band in reciprocal **k**-space.[18]
[d] The time of a fluorophore (NPs/ODs or organic fluorophores) spends in the excited state before emitting a photon and returning to the ground state.
[e] Loss of fluorescence signal due to interactions between the fluorophore and other fluorophores.[41]
[f] When a fluorophore permanently loses the ability to fluoresce due to photon-induced chemical damage and/or covalent bond cleavage.[42]
[g] Size and shape-tunable single crystals of few nm in diameter with quantized energy levels.[21]

biological systems.[15] The potential elimination of toxicological issues and biocompatibility[h] of silicon has prodded silicon as an ideal candidate for *in vivo* cellular imaging and biomolecule tracking agents.

According to the quantum confinement model, PL from nanocrystalline silicon particles has been generally attributed to radiative recombination [in the valence and conduction bands] of excitons[m], where the excitation energy is higher than the optical band energy of the Si NPs.[17] While fast radiative recombination has been frequently observed for semiconductors with direct band gaps, several studies have theorized that freestanding Si particles undergo an indirect to direct band gap transition based on quantum confinement and surface effects.[18,19] This fast radiative recombination exhibited by Si NPs results in sharper, or narrow, emission bands and longer PL lifetimes.

The unique electroluminescent properties of silicon also led to the advancement of solid-state fluorescent sensors for chemical warfare agents and other high-energy compounds (*i.e.* trinitrotoluene (TNT), dinitrotoluene (DNT), nitrobenzene (NB) and other nitroaromatics).[4,5,8] The presence of nitroaromatics can be detected by the photoluminescence (PL) quenching of porous silicon[i]. Upon exposure to nitroaromatics, a dynamic electron transfer between the conduction band of the Si NP to the vacant antibonding molecular orbital (π^*) of the nitroaromatic molecule occurs, resulting in the PL quenching of the Si NPs.[4,5,8,20] This is often referred to as a non-radiative recombination, or Shockley-Read-Hall (SRH) recombination, where an electron falls into a trap caused by lattice distortions or another molecule.[21]

[h] Studies have suggested that silicon can be beneficial to bone and connective tissue health.[43]
[m] Electron-hole-pairs.
[i] Elemental silicon with nanoporous holes in its microstructure.[44]

In recent studies, the PL quenching of Si NPs has also been attributed to aging processes of free standing Si NPs, that is, SiO_2 surface passivation. As freestanding H-Si particles age, a decrease in red-to-NIR (near-infrared) emission and an increase in blue emission is observed.[17,22] Size-inconsistent blue emission from Si NPs with a radius that is closer to the bulk silicon Bohr exciton radius has been frequently reported.[23] While it is characteristic for a Si NP with a diameter of 1-2 nm to exhibit blue emission[14,22,23], which agrees with the effective mass approximation (EMA) calculations, Si NPs with larger radii that exhibit blue emission disagrees with the quantum confinement expectations[1] reported in several papers.[22–24] Several studies have suggested that the blueshifts exhibited by Si NPs with radii larger than 1-2 nm originate from possible nitrogen impurities[24] and/or surface oxidation.[17,22,24,25]

1.2 Electrochemistry of Silicon Nanoparticles

1.2.1 Introduction to Cyclic Voltammetry[26,27]

Cyclic voltammetry (CV) is a versatile electrochemical technique used in modern analytical chemistry. CV can be used to study the electrochemical properties, such as the stability of oxidation states, the number of electrons involved in a reduction-oxidation (redox) process, and the electrochemical reversibility (rate of electron transfer and coupled chemical reactions), of electroactive species. A three-electrode system (Figure 2) is used for a typical CV experiment: a working electrode,

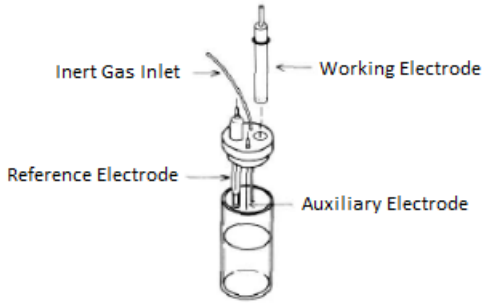

Figure 2. Electrochemical cell with working electrode, auxiliary (counter) electrode, reference electrode, and inert gas inlet for CV.[27]

[1] Quantum confinement model – used to predict electronic and optical properties of materials with diameters of the same magnitude as the de Broglie wavelength of the electron wavefunction.

reference electrode, and an auxiliary electrode (also referred to as a counter electrode). An excitation signal, which is a controlled linear potential, is applied across the working electrode (*e.g.* glassy carbon, platinum, gold, carbon paste, *etc.*) and the reference electrode (*e.g.* SCE[j], Ag/AgCl, *etc.*). The auxiliary electrode (*e.g.* platinum, gold, nickel, *etc.*) provides a current that helps the working electrode sustain electrolysis and prevent large currents from passing through the reference electrode, which could change the potential of the reference electrode.

A positive and negative potential of the working electrode is cycled at an adjusted scan rate between an established potential range, and the potentials are controlled versus a reference electrode. The response signal, *i.e.* the resulting faradaic current at the working electrode, is measured during the potential scan and plotted against the corresponding potential to construct a cyclic voltammogram (Figure 3). Important electrochemical properties of the electroactive species being studied can be obtained from a voltammogram. When a positive potential is applied, the reduced species in the sample medium is oxidized, and an anodic current peak (i_{pa}) at an anodic peak potential (E_{pa}) is observed. As the applied potential is switched to a negative potential, the oxidized species are reduced, and a cathodic current peak (i_{pc}) at an anodic peak potential (E_{pc}) is observed. Mechanistically, an electron transfer between the reduced and oxidized forms of the analyte (*i.e.* electroactive species) and the working electrode is occurring, and the reversibility of the redox process is

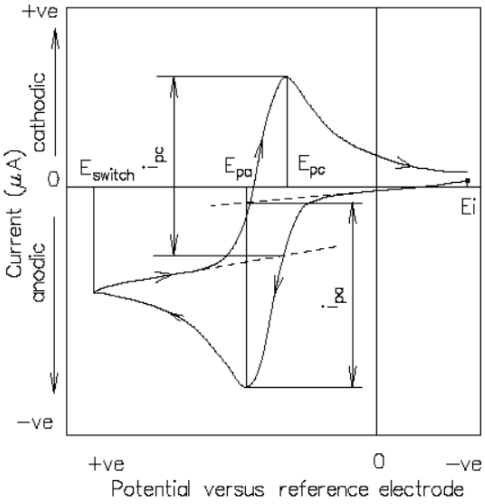

Figure 3. Representative voltammogram with the anodic peak, cathodic peak, anodic peak potential, cathodic peak potential, initial potential, and final (switching) potential labelled.[46]

[j] Saturated calomel electrode; Hg/HgCl.

determined by the rate of the exchanging of electron(s) between the redox couple. The relationship between the potential and the relative concentrations of the [electrochemically reversible] redox couple is governed by the Nernst equation (Eq. 1), as described by

$$E = E^{o\prime} + \frac{RT}{NF}\log_{10}\left(\frac{[Ox]}{[Red]}\right) \quad (1)$$

where E is the applied potential, $E^{o\prime}$ is the formal potential of the redox couple, R is the molar gas constant, T is the temperature in the voltammetric cell, N is the number of electrons transferred, F is the Faraday constant, and $[Ox]$ and $[Red]$ are the relative concentrations of the oxidized and reduced form of the analyte, respectively. The formal potential of the reversible redox couple can be determined by calculating the average of the anodic and cathodic peak potentials, that is

$$E^{o\prime} = \frac{E_{pa}+E_{pc}}{2} \quad (2)$$

The number of electrons (n) being transferred in an electrochemically reversible process can be determined by the separation of the peak potentials, as shown below

$$\Delta E_p = E_{pa} - E_{pc} \cong \frac{0.059}{n} \quad (3)$$

For an electrochemically reversible redox process involving one electron ($n = 1$), the peak separation is approximated to be equal to 0.059 V. An irreversible redox process, however, involves a slow electron transfer at the electrode surface, which would result in an increase in peak separation (*i.e.* $\Delta E_p \gg 0.059$, for a one-electron process). Coupled chemical reactions, or decomposition of the redox couple, can cause electrochemical irreversibility. In an irreversible electrochemical process, a species that is generated during a forward scan [rapidly] reacts with other components in the cell via coupled chemical reactions, causing a decrease in anodic or cathodic peak heights, larger peak potential separation, and/or and

absence in an anodic or cathodic peak.[27] Furthermore, the anodic and cathodic current peaks of [fast] reversible electrochemical processes approach 1 since, in theory, the values of the current peaks are identical. However, quasi-reversible and irreversible processes exhibit deviations from 1 since the peak current ratios are largely influenced by the chemical reactions coupled to the electrode processes.

CV can be used to measure the redox potentials of the analyte of interest, such as ferrocene, Si NPs, and various solvents, as well as the potential window of solvents[k], also known as solvent windows. The HOMO and LUMO energy levels positions of the solvents can be evaluated using CV, where an electron is injected to the LUMO energy level and a hole, or removal of an electron, is added to the HOMO energy level. Electrochemically, the injection of an electron is a reductive process whereas the addition of a hole (removal of an electron) is an oxidative process. The electrochemical band gap energy of a redox active molecule can be measured, where the energy required to oxidize or reduce the molecule is larger enough to overcome Coloumbic (electrostatic) interactions and greater than the HOMO-LUMO separation of the molecule.[26,27]

1.2.2 Solvent Effects on the Photophysical Properties of Si NPs

PL provides information about the ground states in the band gap of the Si NP using defects in the crystal structure of the NP (surface and/or intrinsic), whereas PLE provides information about the absorption and emission of electronic defects in excited states.[28] PLE is a spectroscopic tool that can be used for characterizing optical transitions in semiconductors.[28,29] In a typical PL experiment, when the analyte (Si NP) is excited (energy of the photons from the light source must be larger than the band gap energy), an electron

[k] The potential range between the cathodic and anodic potentials at which the solvent electrolyzes at the electrode.[45]

from a completely filled valence band (referred to as the ground state) is transferred, or excited, into the conduction band—this is referred to as optical band-to-band excitation.[28] Before the electron and hole recombine, that is, when the excited electron relaxes back down to the ground state in the valence band, an intraband relaxation caused by energy transfer to the crystal lattice (excitation of lattice vibrations) occurs.[28] When electron-hole pair annihilation occurs, energy, in the form of photons, is released and produces a characteristic wavelength. This wavelength is lower than the incident wavelength (from the light source) and results in a red shift.

If the redox potential of the quenching species, *i.e.* the solvents, lies within the band gap energy of the Si NPs, a dynamic electron transfer between the redox active molecule (solvent) and the Si NP occurs—this leads to PL quenching of the Si NPs. Thus, by measuring the redox potentials of the solvents, PL quenching of Si NPs by redox active solvent molecules can be predicted.

2. Experimental Section

2.1 Materials

2.1.1 Chemicals. The solvents were dried using the appropriate desiccants and degassed by bubbling argon for 15 minutes. 1-Butanol ($C_4H_{10}O$, 99 % extra pure, ACROS-Fisher Scientific) was dried using activated 0.5 nm molecular sieves; n-butylamine ($C_4H_{11}N$, ≥ 99+ %, ACROS-Fisher Scientific), N,N-dimethylformamide (C_3H_7NO, ≥ 99.8 %, Fisher Scientific), and toluene (C_7H_8, 99.8 %, Sigma Aldrich) were dried using activated 0.4 nm molecular sieves.[30,31] Trichlorosilane ($HSiCl_3$, ≥ 98 %; Alfa Aesar) and electrophoretically pure water (H_2O, > 18 MΩ·cm resistivity, ACROS-Fisher Scientific) were used to prepare the silicon polymer precursor; hydrofluoric acid ($HF_{(aq)}$, 48.0 – 51.0 %, Fisher Science

Education, Hanover Park, IL), ethanol (CH_3CH_2OH, PSU Stockroom), and electrophoretically pure water was used to etch the milled polymer and liberate H-Si particles; toluene ($C_5H_5CH_3$, Purity, MF) was used to extract the H-Si particles; 0.1 M $LiCl/H_2O$ was prepared and used as the supporting electrolyte solution for the cyclic voltammetry studies.

2.1.2 Characterization. The redox potentials of the solvents were measured using a BioLogic SP-200 potentiostat; Shimadzu-RF5310 PC spectrophotometer was used to execute quenching studies on the Si NPs/solvent colloidal solutions; Rigaku Ultima-IV XRD was used to identify the structure of the milled silicon nanocrystalline; ThermoFisher Scientific Nicolet iS5 FT-IR spectrometer, equipped with an iD1 Transmission accessory, was used to characterize the surface of the Si NPs, as-etched.

2.2 Methods[13]

2.2.1 Silicon Nanoparticles Synthesis. Trichlorosilane and nanopure water 1:1.5 (by volume) were added to a deoxygenated 100-mL two-neck round bottom flask and allowed to react under the flow of argon at 0 °C. The hydrochloric acid gas that was produced from the reaction was vented for five days. After venting HCl gas, the sol-gel polymer was removed from the flask and spread onto an evaporation dish to completely dry. The dried polymer was placed into a ceramic boat and annealed at 1100 °C under flowing nitrogen gas in a horizontal tube furnace (Lindberg Blue, Model TF55035A, Lindberg Scientific) for ten hours. The annealed polymer was subsequently ball milled for ten seconds to produce silicon nanocrystalline powder using a tungsten carbide-lined milling vial with two 1-cm tungsten carbide balls and a mill mixer (SPEX 8000M Mixer/Mill, SPEX SamplePrep). The milled

powder was etched using 15 mL of a 1:1:1 (by volume) HF/ethanol/$H_2O_{(aq)}$ solution mixture for 60 minutes to liberate hydride-terminated Si NPs (Figure 4), and the H-Si particles were extracted with 40 mL of dried toluene.

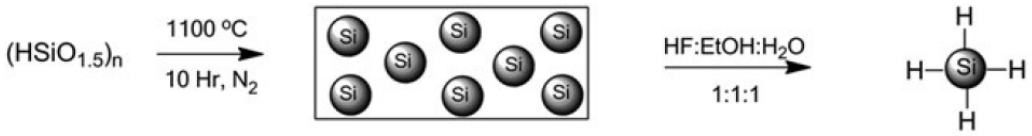

Figure 4. Synthetic procedure for the preparation of H-Si NPs from the $(HSiO_{1.5})_n$ precursor.

2.3 Redox Potential Measurements.[26,32–34]

2.3.1 Conditioning of Electrodes. A three-electrode system is used for the CV experiment. A glassy carbon electrode (area = 7 mm^2), platinum (Pt) coil (area ≈ 0.7 cm^2), and a raw silver wire (99.9% metal basis, ½ hardness, area ≈ 0.12629 in^2, Alfa Aesar) were used as the working, counter, and pseudo-reference electrode, respectively. The working electrode was polished using a 1.0 µm polishing diamond solution, followed by a 0.05 µm polishing alumina solution before and after use. The Pt coil counter electrode was cleaned by running the head of the electrode through an acetylene flame three times, and the Ag wire was polished using aluminum oxide sand paper (9" x 11" 150-grit Al_2O_3, 3M).

2.3.2 Experimental Parameters. A 0.1 M supporting electrolyte solution (1 mL of 0.1 M LiCl) and ferrocene was added to a 10 mL analyte sample. The redox potentials of the samples were measured with a scan rate of 100 mV/s and a forward and reverse potential of ± 3 V. The potential ranges of the solvents were estimated based on previous studies and the optimal potential window was selected based on the initial scan. The starting potential was set at 0.00 V against an open current, and the current was measured over the last 50 % of the step duration and recorded and averaged over 10 voltage steps. The samples were

continuously purged of oxygen by flowing nitrogen gas over the sample in the closed voltammetry cell.

2.3.3 Data Processing. EC-Lab software was used to post-process the data on the voltammogram. The wave function was used to calculate the half-wave potential, and the peak function was used to calculate the anodic and cathodic peak current heights.

2.4 Photoluminescence Measurements

2.4.1 Sample (or Analyte) Preparation. A 5 mM solvent solution (diluted using toluene) was added to 5 mL of freshly etched Si NP extraction and sonicated for 30 seconds. A layer of argon was streamed over each sample vial and stored in the refrigerator to delay aging of the colloids.

2.4.2 Quenching Studies. Three PL and PLE measurements for each colloid sample were taken and averaged. The PL and PLE measurements of the aging particles were immediately taken after dispersing the particles in the solvents (t=0), and the quenching of the aging Si NPs were studied over time.

3. Results and Discussion

3.1 Powder X-Ray Diffraction (PXRD)

Powder x-ray diffraction was run on the annealed and milled $(HSiO_{1.5})_n$ precursor using a Rigaku Ultima IV x-ray diffraction system in parallel geometry. Data was collected from 10° to 60° two theta (2θ), and the reflections for the bulk silicon were calculated, as shown in Figure 5. The intense, broad peak at 2θ = 21.3° (highlighted pink) is indicative of the presence of an amorphous Si phase—the amorphous phase typically exhibits scattered x-rays

that result in a robust, broad peak and is often observed for Si NP precursors.[35,36] The Bragg peaks at 2θ = 28.3°, 48.1°, and 57.5° (highlighted orange regions) are typical x-ray diffraction patterns for polycrystalline Si, with the most intense peak being the (111) reflection at 28.3°. The broadening of the Bragg peaks has been attributed to the deformation of the lattice structure of the crystal, that is, refinement of Si's microstructure. At lower temperatures (< 1400 °C), the peaks become less resolved and decrease in intensity (Figure 6).

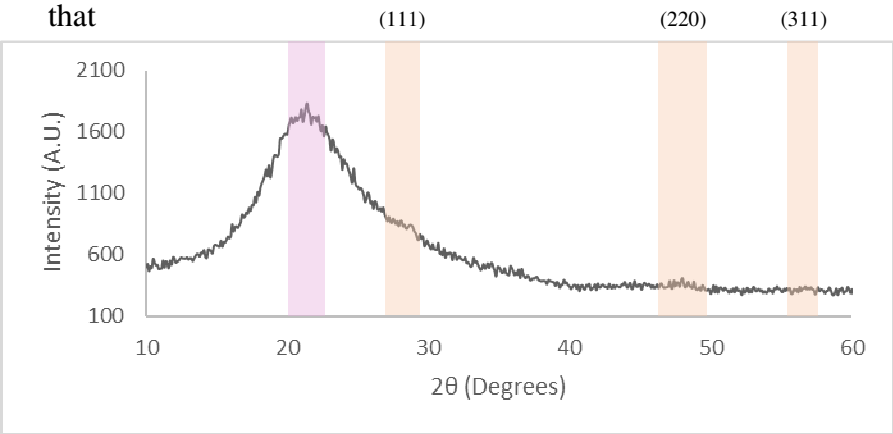

Figure 5. PXRD scan of the annealed (1100 °C) and milled $(HSiO_{1.5})_n$ precursor. The calculated reflections for bulk silicon are highlighted, where the pink highlighted region is indicative of the presence of an amorphous Si phase, and the orange highlighted regions are the Bragg peaks of the bulk silicon (indicative of polycrystalline Si).

As shown in Figure 6, the broadening in the Bragg reflections (peaks) is temperature dependent, that is, the crystal lattice structure becomes deformed as a response to thermal expansion, or thermal movement.[37] While the Bragg peaks are not discrete, the small diffraction peaks corresponding to reflections from the planes (111), (220), and (311) showed that the annealed sol-gel polymer was polycrystalline Si. Furthermore, the obtained PXRD scan from the annealed sol-gel polymer was comparable to past PXRD studies of the $(HSiO_{1.5})_n$ precursor.

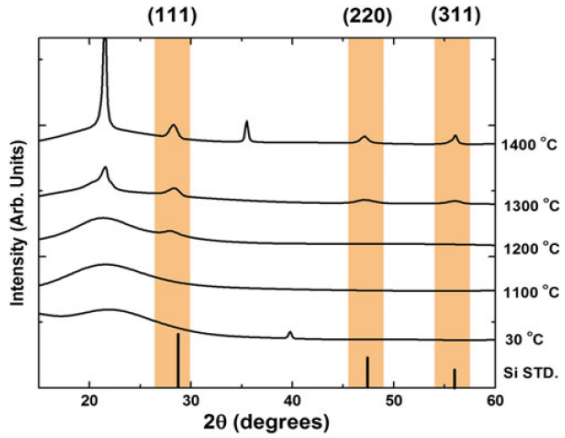

Figure 6. In-situ variable temperature (30 °C - 1400 °C) PXRD study published by Chiu et al.[36]

3.2 FTIR Spectroscopy

Freestanding hydrogen-terminated Si particles (H-Si) were extracted into toluene (40 mL) after chemically etching the annealed and milled sol-gel polymer for 60 minutes using a 15-mL solution of 1:1:1 (by volume) ethanol/water/$HF_{(aq)}$. An aliquot of the Si colloid was concentrated by drying down toluene to obtain ~ 1-2 mL of the colloid. An FTIR spectrum of the as-etched Si NP surface was attained using NaCl plates (salt plates) and a ThermoFisher Scientific Nicolet iS5 FT-IR spectrometer, equipped with an iD1 Transmission accessory, as shown in Figure 7.

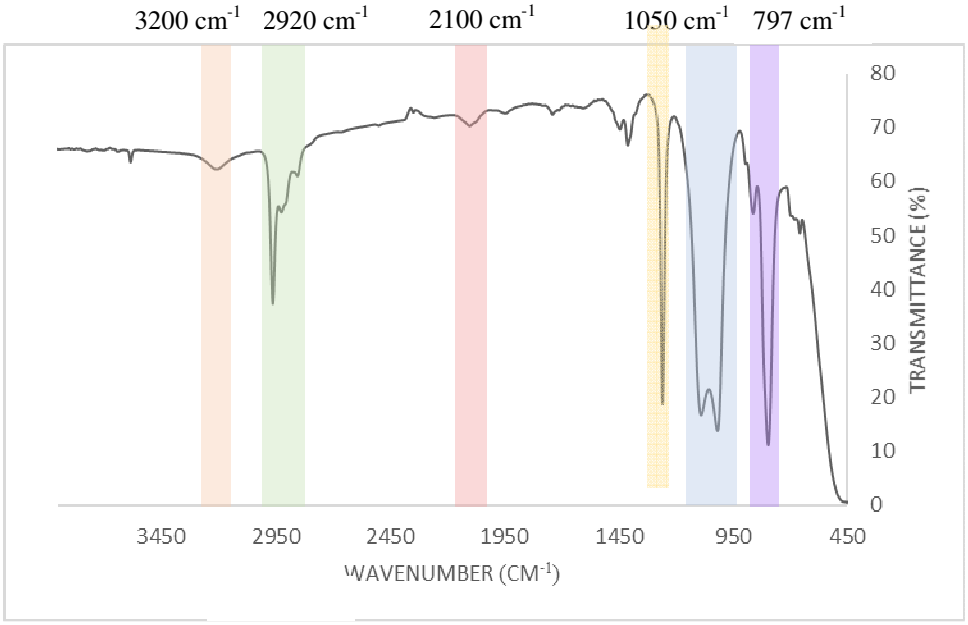

Figure 7. FTIR spectrum of the as-etched Si NPs (H-Si). O-H (orange), C-Hx (green), H-Si (red), Si-O-Si (blue), Si-OH (purple), and Si-C (yellow).

The Si NPs were shown to have hydride, as well as Si-O-Si, Si-OH and Si-C, surface termination by FTIR spectroscopy—a small, broad H-Si stretching at around 2100 cm^{-1}, large Si-O asymmetric vibrations at around 1050 cm^{-1}, large, sharp Si-OH stretch at 797 cm^{-1}, and a Si-C stretch at 1260 cm^{-1} were observed. Residual hydrocarbons (toluene) and a trace amount of water were observed at 2920 cm^{-1} and 3200 cm^{-1}, respectively. Rapid surface

oxidation was observed when the particles were exposed to air when drying off the toluene in the fume hood. Trace amounts of water were most likely introduced during the extraction of the freshly etched Si NPs and/or wet solvent. At around 1260 cm^{-1}, a large, sharp peak indicative of Si-C stretching suggests possible surface adsorption of the toluene on the Si NPs.

3.3 Cyclic Voltammetry

The redox potentials of ferrocene in 1-butanol, n-butylamine, and N,N-dimethylformamide (DMF) were measured using cyclic voltammetry (CV). Representative cyclic voltammograms of ferrocene in 1-butanol, n-butylamine, and DMF are shown in Figures 8 – 10. The voltammograms show that as the applied potential becomes positive, an anodic peak current is observed at the anodic peak potential. As the potential is reversed, that is, as it becomes more negative, a cathodic peak current at the cathodic peak potential is observed. When a positive potential is applied, ferrocene becomes oxidized and is, therefore, converted to ferrocenium. When the potential switches to a more negative potential scan, ferrocenium was converted back to ferrocene. This reversible conversion of ferrocene/ferrocenium is represented below, in Equation 4.

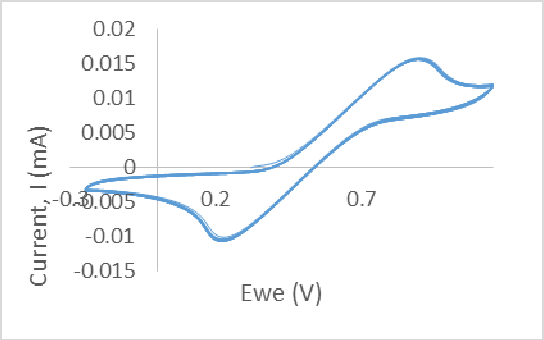

Figure 8. Cyclic voltammogram at the glassy carbon electrode of ferrocene in 1-butanol.

$$Fe(C_5H_5)_2 \leftrightarrow Fe(C_5H_5)_2^+ + e^- \quad (4)$$

The peak and wave analysis functions in the EC-Lab software that was used to post-process the data collected from the voltammograms were used to calculate the anodic and cathodic peak current heights and ratios (i_{pa} and i_{pc}), anodic and cathodic peak potentials (E_{pa}

and E_{pc}), peak potential separation (ΔE_p), and half-wave potentials ($E_{1/2}$), and summarized in Table 1.

Table 1. The anodic/cathodic peak current/potentials, peak current ratios, peak potential separation, and half-wave potentials of ferrocene in 1-butanol, n-butylamine, and DMF.

Solvent	E_{pa} / (V)	E_{pc} / (V)	$\frac{ipa}{ipc}$	ΔE_p / (V)	$E_{1/2}$ / (V)
1-Butanol	0.8985	0.2243	0.9621	0.6742	0.4416
n-Butylamine	0.05243	0.2495	0.1753	0.1971	0.4979
DMF	0.9018	0.6194	0.9931	0.2824	0.7867

Ferrocene is a common redox couple used in electrochemical studies—the oxidation/reduction of ferrocene is a reversible, one-electron process, as shown in Eq. 4. The peak potential separation of ferrocene should, in theory, equal to 0.059 since the redox process involves only one electron. The peak potential separation of ferrocene in 1-butanol was calculated to be 0.6742 V, which implied that the oxidation/reduction of ferrocene in 1-butanol did not involve one electron, thus was not electrochemically reversible. The large peak potential separation of ferrocene in 1-butanol suggested that a slow electron exchange of the redox couple with the glassy carbon occurred. The anodic/cathodic peak current ratio of ferrocene in 1-butanol was calculated to be close to 1.00—this means that the anodic and cathodic peak current heights were nearly identical, a characteristic that is most commonly observed for fast, reversible redox processes. The half-wave potential of ferrocene in 1-butanol was reported to be 0.4416 V. These results, however, were largely affected by the type of supporting

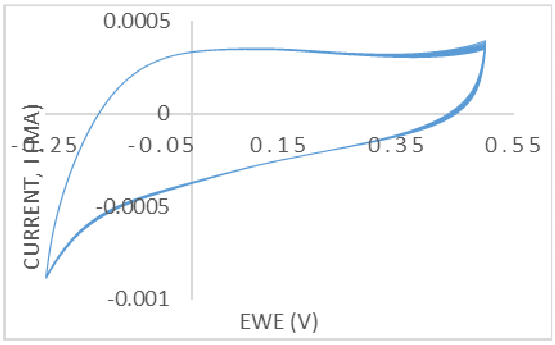

Figure 9. Cyclic voltammogram at the glassy carbon electrode of ferrocene in n-butylamine.

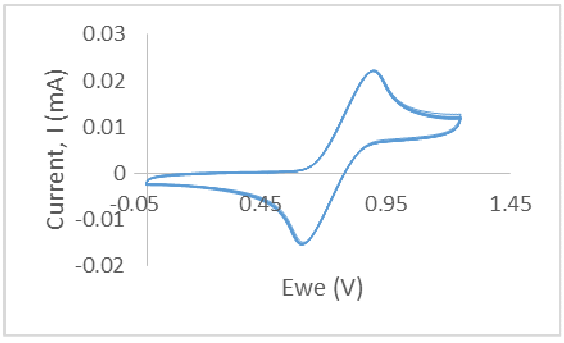

Figure 10. Cyclic voltammogram at the glassy carbon electrode of ferrocene in DMF.

electrolyte used. A 0.1 M LiCl and water solution (1.0 mL) was used as the supporting electrolyte for this study—the measured redox potentials of the solvents were speculated to be the redox potentials of water. Water and chloride are electrochemically unstable, thus the use of water and a chloride salt in the solvent medium drastically affected the redox of the solvents.

The peak potential separation of ferrocene in DMF was calculated to be 0.2824 V. The anodic/cathodic peak current ratio was reported to be 0.9931, and the half-wave potential was measured to be 0.7867 V. A previous study on CV of ferrocene in DMF, published by Tsierkezos, reported peak current ratios, peak potential separation, and half-wave potentials of 0.96, 0.086 V, and 0.951 V, respectively.[38] The large deviation of the peak potential separation of ferrocene in DMF from 0.059 V is consistent with the speculation that water and chloride greatly affected the measurements obtained from the voltammogram. Ferrocene in DMF was determined to be a quasi-reversible electrochemical process, albeit the measured values deviated from the values reported by Tsierkezos and the expected values for a fast, reversible redox process for a single electron transfer (Nernst equation).

The peak potential separation, anodic/cathodic peak current ratio, and half-wave potential of ferrocene in n-butylamine was calculated to be 0.1971 V, 0.1753, and 0.4979 V, respectively. An irreversible electrochemical process was observed based on the absence of an anodic and cathodic peak in the voltammogram of ferrocene in n-butylamine, as shown in Figure 9. The absence of an anodic and cathodic peak was speculated to be due to coupled chemical reactions at the surface of the glassy carbon electrode and dissolved O_2 in the sample medium. As the potential was cycled, a gradual shift in the anodic peak was observed, illustrating the decomposition of n-butylamine and an increase in ferrocenium ions.

The anodic peak indicated that, as a positive potential was applied, ferrocene was being converted to ferrocenium. However, as the potential was switched to a more negative potential, ferrocenium was not being converted back to ferrocene, which resulted the anodic peak to shift and increase in peak height.

The measured half-wave potentials, or the redox potentials, of ferrocene in 1-butanol, DMF, and n-butylamine could not be used to determine the electrochemical behavior of these solvents. The main source of error was the use of chloride ions and water, which are very electrochemically active molecules. Furthermore, the redox potentials of ferrocene in the solvents doesn't mean anything in the context of Si NPs. However, this CV study could aid in designing an experiment where the electrochemical behavior of Si NPs in various solvents are studied, where ferrocene can be used as a reference peak. By using ferrocene as a reference, the reversibility and the number of electrons involved in the redox process of Si NPs can be studied with more ease and make the voltammograms less complex.

3.4 Photoluminescence Quenching Studies

The photoluminescence quenching capabilities of DMF, 1-butanol, and n-butylamine on H-terminated Si NPs were studied. These solvents (Figure 11) were chosen based on their varying electron-withdrawing or electron-donating properties.

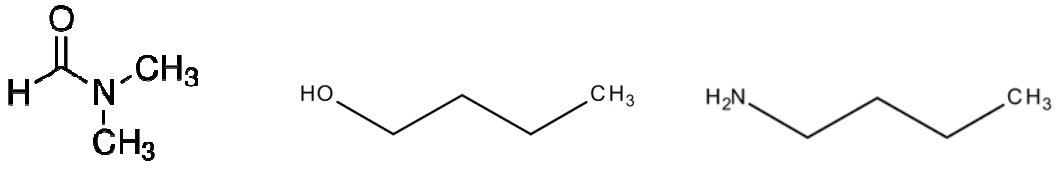

(a) (b) (c)

Figure 11. Molecular structures of N,N-dimethylformamide (a), 1-butanol (b), and n-butylamine (c). (Images provided by PubChem (NIH).[47]

The freshly-etched H-Si particles were dispersed in a 5 mM solvent solution, and photoluminescence (PL) and photoluminescence excitation (PLE) measurements were taken immediately after dispersal (time, t = 0) and as the particles aged (time (in hours), t = 22 and 43). Three scans per PL and PLE measurement were taken and averaged for each sample. Duplicate samples were prepared in order to see if the study would be reproducible. The PL and PLE scans of the as-etched H-Si particles, when t (hours) = 0, 22, and 43 were superimposed for each solvent (Figures 12 – 17).

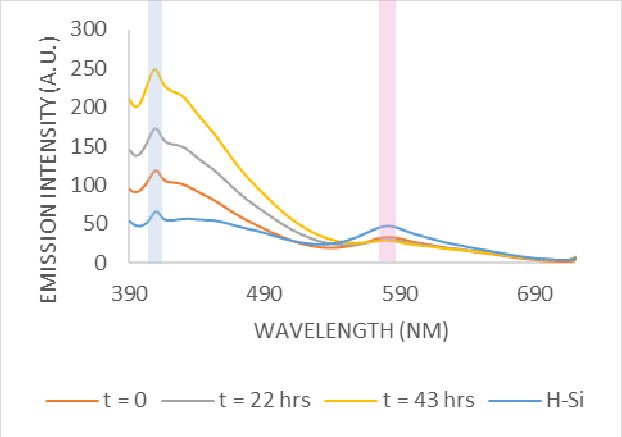

Figure 12. Superimposed PL measurements of H-Si particles (as etched) and after dispersal in 1-butanol at time (in hours), t = 0, 22, and 43.

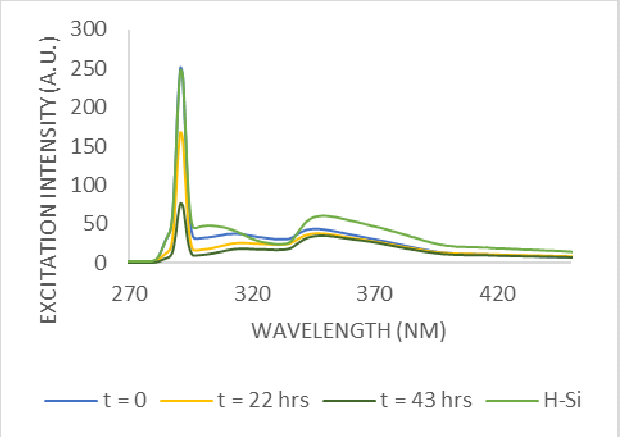

Figure 13. Superimposed PLE measurements of H-Si particles (as etched) and after dispersal in 1-butanol at time (in hours), t = 0, 22, and 43.

Figure 12 shows the emission spectra of the as-etched H-Si particles in toluene (blue), H-Si particles in 1-butanol immediately after dispersion (orange), and aged H-Si particles in 1-butanol after 22 (grey) and 43 (yellow) hours. The as-etched particles exhibited characteristic red emission [at 581 nm] under 365-nm excitation, and after immediate dispersion in 1-butanol, a rapid decrease in PL intensity at 581 nm and steady increase in PL at 411 nm was detected. After 22 hours, a noticeable red-to-blue PL conversion—that is, an increase in blue emission and a decrease in red emission—was observed. After 43 hours, the Si NPs were quenched, signifying that the particles no longer emitted red. Figure 13 shows the excitation spectra of the as-etched H-Si particles in toluene (light green), H-Si particles in 1-butanol

immediately after dispersion (blue), and aged H-Si particles in 1-butanol after 22 (yellow) and 43 (dark green) hours. The as-etched Si NPs showed strong excitations at 292 nm, and as the particles aged, the intensity of the peaks gradually decreased.

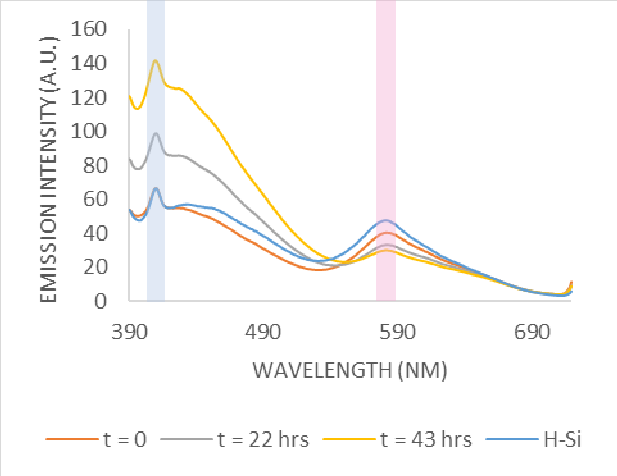

Figure 14. Superimposed PL measurements of H-Si particles (as etched) and after dispersal in n-butylamine at time (in hours), t = 0, 22, and 43.

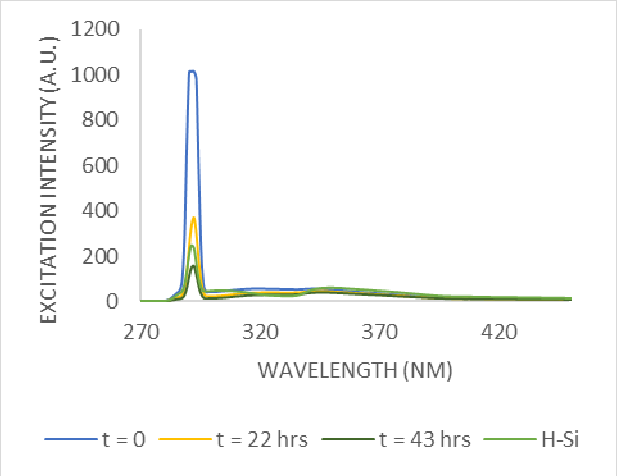

Figure 15. Superimposed PLE measurements of H-Si particles (as etched) and after dispersal in n-butylamine at time (in hours), t = 0, 22, and 43.

Figure 14 shows the emission spectra of the as-etched H-Si particles in toluene (blue), H-Si particles in n-butylamine immediately after dispersion (orange), and aged H-Si particles in 1-butanol after 22 (grey) and 43 (yellow) hours. The PL intensity of the Si NPs dispersed in n-butylamine was weaker with a slower onset of red-to-blue PL conversion. Figure 15 shows the excitation spectra of the as-etched H-Si particles in toluene (light green), H-Si particles in n-butylamine immediately after dispersion (blue), and the aged H-Si particles after 22 (yellow) and 43 (dark green) hours. Immediately after dispersion in n-butylamine, an increase in PLE intensity and a rapid decay after 22 hours at 292 nm was observed.

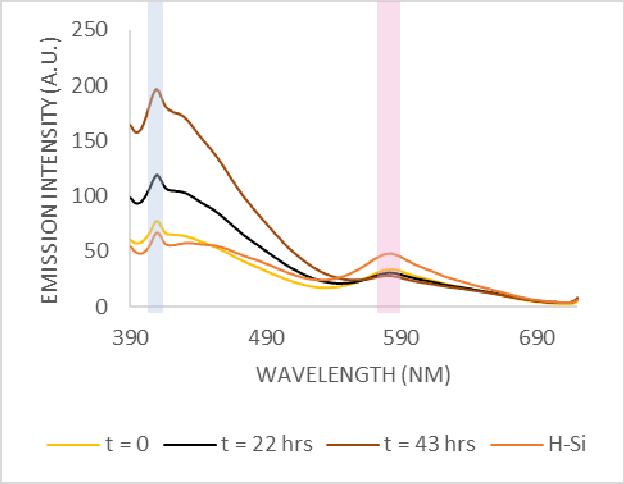

Figure 16. Superimposed PL measurements of H-Si particles (as etched) and after dispersal in N,N-dimethylformamide (DMF) at time (in hours), t = 0, 22, and 43.

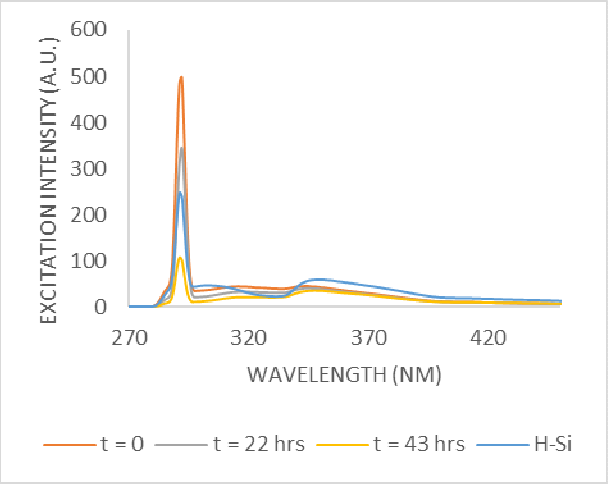

Figure 17. Superimposed PLE measurements of H-Si particles (as etched) and after dispersal in N,N-dimethylformamide (DMF) at time (in hours), t = 0, 22, and 43.

Figure 16 shows the emission spectra of the as-etched H-Si particles in toluene (orange), H-Si particles in DMF immediately after dispersion (yellow), and aged H-Si particles in DMF after 22 (black) and 43 (brown) hours. Immediately after dispersal, a decrease in PL intensity was also observed, however, only a slight increase in blue emission was detected. After 22 and 43 hours, the PL of the Si NPs was quenched, and a large blue conversion was measured. Figure 17 shows the excitation spectra of the as-etched H-Si particles in toluene (blue), H-Si particles in DMF immediately after dispersion (orange), and the aged H-Si particles after 22 (grey) and 43 (yellow) hours. A steady decrease in excitation at 292 nm was measured, similar to the Si NPs dispersed in 1-butanol.

The PL spectrum of the as-etched Si NPs exhibited a relatively narrow and sharp peak at 581 nm, which is characteristic of red-emitting hydride-terminated Si NPs. In addition to the red emission at 581 nm, a strong blue emission at 411 nm was also observed. The origin of blue PL from the Si NPs has been one of the most controversial issues, however several studies have suggested that the blue PL exhibited by the Si NPs originates from oxygen

passivation on the Si NP surfaces.[15,17,22,24,25,39] Other studies have suggested that blue PL from the Si NPs is attributed to the indirect-to-direct band gap transition in small Si NPs (1-2 nm).[24]

After dispersing the particles in 1-butanol, n-butylamine, and DMF, broadening and a decrease in PL intensity of the emission peak at 581 nm was observed. As the particles aged, a discernable red-to-blue PL conversion was measured, and after 43 hours, red PL of the Si NPs was quenched. Hydride-terminated Si NPs are unstable and very reactive—the H-Si particles become susceptible to surface oxidation, and upon exposure to air (or oxygen sources), Si=O bonds are easily formed. This oxygen passivation of the Si NP surfaces caused blue PL conversions *via* electron-hole annihilation (recombination), which involved a trapped electron or exciton. As the oxide layer on the Si NP surfaces grow, the core diameter of the particles decrease.

The Si NPs dispersed in 1-butanol exhibited greater blue PL intensity versus the particles dispersed in n-butylamine and DMF. After 43 hours, the blue emission intensity of the particles in 1-butanol was around 246. This high blue PL intensity can be attributed to oxygen sources from 1-butanol in addition to oxygen passivation from the exposure to air when the sample was transferred to the cuvette. Similar to 1-butanol, the particles in DMF also exhibited greater blue PL intensity at around 195. Furthermore, both 1-butanol and DMF were more nucleophilic relative to n-butylamine. Although DMF has two electron-rich atoms (O and N), the nitrogen stabilizes the electron-withdrawing inductive effects of the oxygen in the molecule. The Si NPs dispersed in n-butylamine resulted in a weaker blue PL intensity after 43 hours, however the red PL of the particles were, regardless, quenched.

4. Conclusions

The effects of using solvents with varying redox potentials on the optical properties of hydride terminated Si NPs were studied. CV was used to measure the redox potentials of ferrocene in 1-butanol, n-butylamine, and DMF as well as the relative solvent windows. However, a few experimental conundrums were encountered when measuring the half-wave potentials of the solvents due to the use of chloride ions and water, which are two electroactive molecules. PL and PLE was used to study the PL quenching capabilities of the solvents on hydride-terminated Si NPs, where [complete] quenching of the PL from the Si NPs dispersed in the solvents was observed after 43 hours. The solvents with oxygen sources, namely 1-butanol and DMF, exhibited greater effects on the optical properties of Si NPs due to their increasing nucleophilicity relative to n-butylamine.

5. Appendix

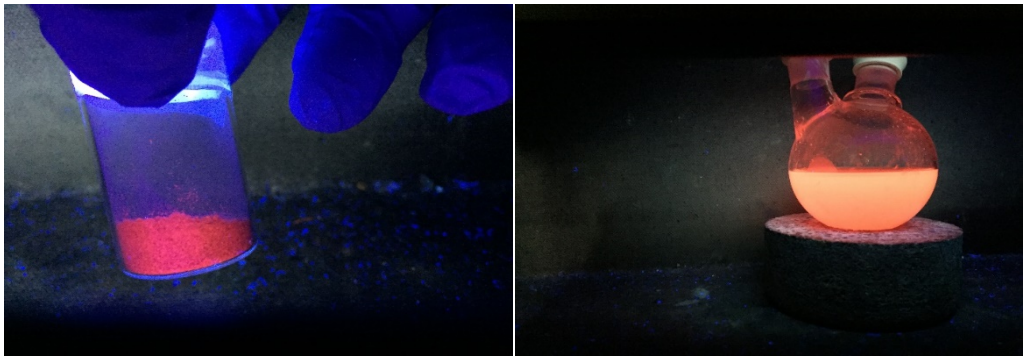

Figure 18. Annealed and milled $(HSiO_{1.5})_n$ precursor fluoresces bright red under 365-nm using a hand-held UV lamp (left). Freshly etched H-Si particles extracted into toluene fluoresced bright red-orange under 365-nm using a hand-held UV lamp (right).

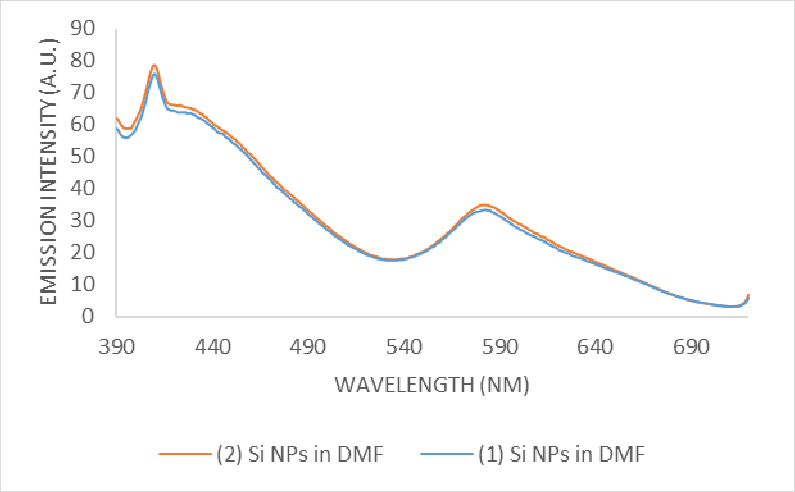

Figure 19. The two replicates of the Si NPs dispersed in 5 mM DMF exhibited comparable intensities.

6. References

(1) Wang, E. C.; Wang, A. Z. Nanoparticles and their applications in cell and molecular biology. *Integr. Biol. (Camb).* **2014**, *6*, 9–26 DOI: 10.1039/c3ib40165k.

(2) Horikoshi, S.; Serpone, N. Introduction to Nanoparticles. In *Microwaves in Nanoparticle Synthesis*; Wiley-VCH, 2013; pp 1–24.

(3) Park, J.-H.; Gu, L.; von Maltzahn, G.; Ruoslahti, E.; Bhatia, S. N.; Sailor, M. J. Biodegradable luminescent porous silicon nanoparticles for in vivo applications. *Nat. Mater.* **2009**, *8* (4), 331–336 DOI: 10.1038/nmat2398.

(4) Content, S.; Trogler, W.; Sailor, M. Detection of nitrobenzene, DNT, and TNT vapors by quenching of porous silicon photoluminescence. *Chem. Eur. J.* **2000**, *6* (12), 2205–2213 DOI: 10.1002/1521-3765(20000616)6:12<2205::AID-CHEM2205>3.0.CO;2-A.

(5) Sailor, M. J.; Wu, E. C. Photoluminescence-based sensing with porous silicon films, microparticles, and nanoparticles. *Adv. Funct. Mater.* **2009**, *19* (20), 3195–3208 DOI: 10.1002/adfm.200900535.

(6) Gao, X.; Yang, L.; Petros, J. a.; Marshall, F. F.; Simons, J. W.; Nie, S. In vivo molecular and cellular imaging with quantum dots. *Curr. Opin. Biotechnol.* **2005**, *16*, 63–72 DOI: 10.1016/j.copbio.2004.11.003.

(7) Wang, G.; Yau, S. T.; Mantey, K.; Nayfeh, M. H. Fluorescent Si nanoparticle-based electrode for sensing biomedical substances. *Opt. Commun.* **2008**, *281* (7), 1765–1770 DOI: 10.1016/j.optcom.2007.07.070.

(8) Gonzalez, C. M.; Iqbal, M.; Dasog, M.; Piercey, D. G.; Lockwood, R.; Klapötke, T. M.; Veinot, J. G. C. Detection of high-energy compounds using photoluminescent silicon

nanocrystal paper based sensors. *Nanoscale* **2014**, *6* (5), 2608–2612 DOI: 10.1039/c3nr06271f.

(9) Chang, H.; Sun, S.-Q. Silicon nanoparticles: Preparation, properties, and applications. *Chinese Phys. B* **2014**, *23* (8), 088102 DOI: 10.1088/1674-1056/23/8/088102.

(10) Jovin, T. M. Quantum dots finally come of age. *Nat. Biotechnol.* **2003**, *21* (1), 32–33 DOI: 10.1038/nbt0103-32.

(11) Chang, Y.-P.; Pinaud, F.; Antelman, J.; Weiss, S. Tracking bio-molecules in live cells using quantum dots. *J. Biophotonics* **2012**, *29* (6), 997–1003 DOI: 10.1016/j.biotechadv.2011.08.021.Secreted.

(12) Chan, W. C. W.; Maxwell, D. J.; Gao, X.; Bailey, R. E.; Han, M.; Nie, S. Luminescent quantum dots for multiplexed biological detection and imaging. *Curr. Opin. Biotechnol.* **2002**, *13* (1), 40–46 DOI: 10.1016/S0958-1669(02)00282-3.

(13) Chiu, S.; Manhat, B. A.; Debenedetti, W. J. I.; Brown, A. L. Aqueous red-emitting silicon nanoparticles for cellular imaging : Consequences of protecting against surface passivation by hydroxide and water for stable red emission. **2012**, 23–31 DOI: 10.1557/jmr.2012.377.

(14) Farrell, N. O. Silicon nanoparticles : applications in cell biology and medicine. **2006**, *1* (4), 451–472.

(15) Warner, J. H.; Hoshino, A.; Yamamoto, K.; Tilley, R. D. Water-soluble photoluminescent silicon quantum dots. *Angew. Chemie - Int. Ed.* **2005**, *44* (29), 4550–4554 DOI: 10.1002/anie.200501256.

(16) Derfus, A. M.; Chan, W. C. W.; Bhatia, S. N. Probing the Cytotoxicity of Semiconductor Quantum Dots. *Nano Lett.* **2004**, *4* (1), 11–18 DOI: 10.1021/nl0347334.

(17) Nesheva, D.; Raptis, C.; Perakis, a.; Bineva, I.; Aneva, Z.; Levi, Z.; Alexandrova, S.; Hofmeister, H. Raman scattering and photoluminescence from Si nanoparticles in annealed SiO x thin films. *J. Appl. Phys.* **2002**, *92* (8), 4678–4683 DOI: 10.1063/1.1504176.

(18) Seo, D.; Hoffmann, R. Direct and indirect band gap types in one-dimensional conjugated or stacked organic materials. *Theor. Chem. Accounts Theory, …* **1999**, *102*, 23–32 DOI: 10.1007/s00214980m136.

(19) Lin, L.; Li, Z.; Feng, J.; Zhang, Z. Indirect to direct band gap transition in ultra-thin silicon films. *Phys. Chem. Chem. Phys.* **2013**, *15*, 6063–6067 DOI: 10.1039/c3cp50429h.

(20) Rehm, J. M.; McLendon, G. L.; Fauchet, P. M. Conduction and valence band edges of porous silicon determined by electron transfer. *J. Am. Chem. Soc.* **1996**, *118* (18), 4490–4491 DOI: 10.1021/ja9538795.

(21) Michalet, X.; Pinaud, F.; Bentolila, L. A.; Tsay, J. M.; Doose, S.; Li, J. J.; Sundaresan, G.; Wu, A. M.; Gambhir, S. S.; Weiss, S. Quantum Dots for Live Cells, in Vivo Imaging, and Diagnostics. *Sci. Mag* **2013**, *307* (5709), 538–545 DOI: 10.1126/science.1104274.

(22) Chen, H. S.; Chiu, J. J.; Perng, T. P. On the photoluminescence of Si nanoparticles. *Mater. Phys. Mech.* **2001**, *4*, 62–66.

(23) Chiu, S.-K.; Manhat, B. A.; Debenedetti, W. J. I.; Brown, A. L.; Fichter, K.; Vu, T.; Eastman, M.; Jiao, J.; Goforth, A. M. Aqueous red-emitting silicon nanoparticles for cellular imaging: Consequences of protecting against surface passivation by hydroxide and water for stable red emission. **2013** DOI: 10.1557/jmr.2012.377.

(24) Dasog, M.; Yang, Z.; Atkins, T. M.; Faramus, A.; Singh, M. P.; Muthuswamy, E.; Kauziarich, S. M.; Tilley, R. D.; Veinot, J. G. C. Chemical Insight Into The Origina of Red and Blue Photoluminescence Arising From Freestanding Silicon Nanocrystals. *ACS Nano* **2012**, *29* (6), 997–1003 DOI: 10.1016/j.biotechadv.2011.08.021.Secreted.

(25) Canham, L. T.; Loni, A.; Calcott, P. D. J.; Simons, A. J.; Reeves, C.; Houlton, M. R.; Newey, J. P.; Nash, K. J.; Cox, T. I. On the origin of blue luminescence ariding from atmospheric impregnation of oxidized porous silicon. *Thin Solid Films* **1996**, 112–115.

(26) Van Benschoten, J. J.; Lewis, J. Y.; Heineman, W. R.; Roston, D. a.; Kissinger, P. T. Cyclic voltammetry experiment. *J. Chem. Educ.* **1983**, *60* (9), 772 DOI: 10.1021/ed060p772.

(27) Kissinger, P. T.; Heineman, W. R. Cyclic voltammetry. *J. Chem. Educ.* **1983**, *60* (9), 702 DOI: 10.1021/ed060p702.

(28) Hannewald, K.; Glutsch, S.; Bechstedt, F. Nonequilibrium theory of photoluminescence excitation spectroscopy in semiconductors. *Phys. Status Solidi Basic Res.* **2003**, *238* (3), 517–520 DOI: 10.1002/pssb.200303178.

(29) Townshen, a. *Principles of Instrumental Analysis*; 1983; Vol. 152.

(30) Williams, D. B. G.; Lawton, M. Drying of Organic Solvents□: Quantitative Evaluation of the Efficiency of Several Desiccants. **2010**, 8351–8354 DOI: 10.1021/jo101589h.

(31) Armarego, Wilfred L. F., Chai, C. L. L. *Purification of Laboratory Chemicals*, 6th ed.; Elsevier Inc.: Burlington, 2009.

(32) BioLogic Science Instruments. EC-Lab Software User ’s Manual. **2013**, No. July.

(33) BioLogic Science Instruments. EC-Lab Software: Techniques and Applications. **2013**, No. March.

(34) BioLogic Science Instruments. F CT series User ’s Manual. **2010**, No. September.

(35) Odo, E. a; Britton, D. T.; Gonfa, G. G.; Harting, M.; State, O.; Town, C.; Africa, S.; Dawa, D. Structure and Characterization of Silicon Nanoparticles Produced Using a Vibratory Disc Mill. **2012**, 45–56.

(36) Chiu, S.-K.; Manhat, B. a.; DeBenedetti, W. J. I.; Brown, A. L.; Fichter, K.; Vu, T.; Eastman, M.; Jiao, J.; Goforth, A. M. Aqueous red-emitting silicon nanoparticles for cellular imaging: Consequences of protecting against surface passivation by hydroxide and water for stable red emission. *J. Mater. Res.* **2013**, *28* (02), 216–230 DOI: 10.1557/jmr.2012.377.

(37) La Fleur, P. L. The temperature dependence of X-ray diffraction intensities of crystals. *J. Int. Union Crystallogr.* **1970**, *26* (6), 674–678.

(38) Tsierkezos, N. G. Cyclic voltammetric studies of ferrocene in nonaqueous solvents in the temperature range from 248.15 to 298.15 K. *J. Solution Chem.* **2007**, *36* (3), 289–302 DOI: 10.1007/s10953-006-9119-9.

(39) Kanemitsu, Y. Visible Luminescence from oxidized Si nanometer-sized spheres: Exciton confinement on a sperical shell. *Am. Phys. Soc.* **1993**, *48*, 4883–4886.

(40) Kumar, M.; Sarin, S. K. Biomarkers of diseases in medicine. *Curr. Trends Sci.* **2010**, *15*, 403–4017.

(41) Tae, W. K.; Park, J. H.; Hong, J. I. Self-quenching mechanism: The influence of quencher and spacer on quencher-fluorescein probes. *Bull. Korean Chem. Soc.* **2007**, *28* (7), 1221–1223 DOI: 10.5012/bkcs.2007.28.7.1221.

(42) Zheng, Q.; Blanchard, S. C. Single Fluorophore Photobleaching. *Encyclopedia of Biophysics*; 2013; pp 2324–2326.

(43) Jugdaohsingh, R. Silicon and bone health. *J. Nutr. Health Aging* **2009**, *11* (2), 99–110.

(44) Lee, G. Y. Small is Big: Studying Silicon Nanotechnology at UCSD. *Imagine* **2014**, 21–23.

(45) Maeshima, H.; Fisher, C. A. J.; Kuwabara, A.; Moriwake, H. Electrochemical Potential Windows of Supercapacitor Electrolytes from First-Principles Calculations. **2010**, *2*, 198–199.

(46) Brodovitch, J.-C. *The Oxidation of Ferrocene: A Cyclic Voltammetry Experiment*; 2012.

(47) National Institute of Health. PubChem.